Structural LES modeling with high-order spectral difference schemes

By G. Lodato, P. Castonguay AND A. Jameson

1. Motivation and objectives

Notwithstanding the considerable effort which has been devoted to the development of accurate and relatively reliable sub-grid scale (SGS) models for LES, in most cases, the underlying numerical methods, which are available within the framework of industrial CFD applications, generally rely upon highly dissipative schemes. The inherent numerical dissipation introduced by such numerical schemes limits their ability to correctly represent the high-frequency end of the spectrum resolved in LES.

Hence it is necessary to combine high-order numerical schemes with advanced SGS modeling techniques in order for LES to become a valuable and reliable tool for fundamental flow physics and industrial applications. Unfortunately, most of the available high-order numerical schemes are designed to be used on cartesian or very smooth structured curvilinear meshes and therefore they are inadequate to simulate turbulent flows over complex geometries. In the current work, a high-order unstructured solver is combined with an explicit filtering LES method, thus allowing highly accurate turbulent flow computations on realistic geometries that were previously possible only with low-order schemes.

High-order numerical schemes for solving the compressible Navier-Stokes equations on unstructured grids have been widely studied during the last decade. By far the most mature and widely used of these schemes are based on the Discontinuous Galerkin (DG) method (Hesthaven & Warburton 2007; Karniadakis & Sherwin 1999). However, several alternative high-order methods have recently been proposed, including Spectral Difference (SD) type schemes (Kopriva & Kolias 1996; Huynh 2007; Liu *et al.* 2006; May & Jameson 2006; Sun *et al.* 2007; Wang *et al.* 2007; Liang *et al.* 2009*a*), which potentially offer increased efficiency compared with DG methods (as well as being simpler to implement). The SD method has been successfully applied to viscous compressible flows with shocks (Premasuthan *et al.* 2009), implicit LES of turbulent channel flow (Liang *et al.* 2009*c*) and flow around circular cylinders (Liang *et al.* 2009*b*; Mohammad *et al.* 2010; Ou *et al.* 2009), as well as transitional flows over an SD7003 airfoil (Castonguay *et al.* 2010). The combination of the SD method with SGS modeling techniques for explicit LES, on the other hand, has not been widely studied. Parsani *et al.* (2010) obtained encouraging results using the WALE (Nicoud & Ducros 1999) eddy-viscosity model but their analysis was restricted to two-dimensional flows, and thus was not fully physically relevant.

Within the framework of the SD method for three-dimensional unstructured hexahedral grids, the present study addresses the implementation of a structural SGS model based on the scale similarity assumption (Bardina *et al.* 1980), namely the WALE Similarity Mixed model proposed by Lodato *et al.* (2009). To the authors' knowledge, this represents the first implementation of a structural SGS model in a three-dimensional solver that uses the SD method. Moreover, the proposed implementation of a constrained

discrete filter of arbitrary order for the SD method will be suitable for any other explicit filtering SGS approach.

2. Mathematical formulation

2.1. *The numerical scheme*

In the present work, the Navier-Stokes equations are solved using the high-order unstructured SD method for spatial discretization. The formulation of the equations on hexahedral grids is similar to the formulation by Sun *et al.* (2007), which will be summarized below for completeness. After introducing the *bar* filter operator and the density-weighted Favre filter operator *tilde*, the unsteady compressible Navier-Stokes equations in conservative form are written as

$$\frac{\partial \overline{\boldsymbol{U}}}{\partial t} + \frac{\partial \overline{\boldsymbol{F}}^k}{\partial x_k} = \boldsymbol{0}, \tag{2.1}$$

where $\overline{\boldsymbol{U}} = \begin{pmatrix} \overline{\rho} & \overline{\rho u_1} & \overline{\rho u_2} & \overline{\rho u_3} & \overline{\rho e} \end{pmatrix}^{\mathrm{T}}$ is the vector of conservative variables, and $\overline{\boldsymbol{F}}^k = \overline{\boldsymbol{F_I}}^k - \overline{\boldsymbol{D}}^k$ accounts for the inviscid and viscous flux vectors, which are defined as

$$\overline{\boldsymbol{F_I}}^k = \begin{pmatrix} \overline{\rho u}_k \\ \overline{\rho u}_1 \widetilde{u}_k + \delta_{1k}\overline{\varpi} \\ \overline{\rho u}_2 \widetilde{u}_k + \delta_{2k}\overline{\varpi} \\ \overline{\rho u}_3 \widetilde{u}_k + \delta_{3k}\overline{\varpi} \\ (\overline{\rho e} + \overline{\varpi})\widetilde{u}_k \end{pmatrix}, \quad \overline{\boldsymbol{D}}^k = \begin{pmatrix} 0 \\ 2\overline{\mu}\widetilde{A}_{1k} + \tau^{\mathrm{d}}_{1k} \\ 2\overline{\mu}\widetilde{A}_{2k} + \tau^{\mathrm{d}}_{2k} \\ 2\overline{\mu}\widetilde{A}_{3k} + \tau^{\mathrm{d}}_{3k} \\ 2\overline{\mu}\widetilde{u}_j\widetilde{A}_{kj} + \frac{\overline{\mu}c_p}{Pr}\frac{\partial \widetilde{\vartheta}}{\partial x_k} + q_k \end{pmatrix}, \tag{2.2}$$

where ρ is the fluid's density, u_k is the velocity vector, e is the total energy (internal + kinetic), μ is the dynamic viscosity, A_{ij} is the deviator of the deformation tensor, c_p is the specific heat capacity at constant pressure and Pr is the Prandtl number. In particular, $\overline{\varpi}$ and $\widetilde{\vartheta}$ are the filtered *macro-pressure* and *macro-temperature*, and these quantities are related by the usual equation of state, i.e., $\overline{\varpi} = \overline{\rho} R \widetilde{\vartheta}$ (see Lesieur *et al.* 2005; Lodato *et al.* 2009 for a details about the underlying hypotheses). τ_{ij} and q_k in Eq. (2.2) represent the usual unclosed SGS terms (note that the superscript 'd' refers to the deviatoric part of the relevant tensor).

To achieve an efficient implementation, all elements in the physical domain are transformed to a standard cubic element described by local coordinates $\boldsymbol{\xi} = (\xi_1, \xi_2, \xi_3)$, with $\boldsymbol{\xi} \in [0:1]^3$. The governing equations in the physical domain are then transferred into the computational domain, and they take the form

$$\frac{\partial \overline{\boldsymbol{\mathcal{U}}}}{\partial t} + \frac{\partial \overline{\boldsymbol{\mathcal{F}}}^k}{\partial \xi_k} = \boldsymbol{0}, \tag{2.3}$$

where

$$\overline{\boldsymbol{\mathcal{U}}} = |\det(J)|\overline{\boldsymbol{U}} \quad \text{and} \quad \overline{\boldsymbol{\mathcal{F}}}^k = |\det(J)|\frac{\partial \xi_k}{\partial x_j}\overline{\boldsymbol{F}}^j, \tag{2.4}$$

and $\det(J)$ represents the determinant of the Jacobian matrix $J_{ij} = \partial x_i / \partial \xi_j$.

Within each standard element, two sets of points are defined, namely, the solution points and the flux points, as schematically illustrated in Figure 1 for a one-dimensional element. In order to construct a degree $(N-1)$ polynomial for each coordinate direction, the solution at N points is required. These N points in 1D are chosen to be the Gauss-

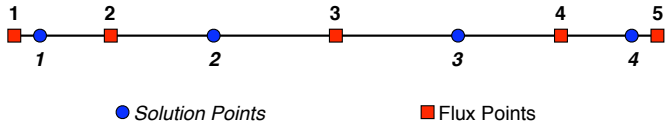

FIGURE 1. Schematic representation of the one dimensional distribution of solution and flux points within the SD element for $N = 4$.

Legendre quadrature points, whereas the flux points were selected to be the Gauss-Legendre quadrature points of order $N-1$ plus the two end points 0 and 1. Using the N solution points and the $N+1$ flux points, polynomials of degree $N-1$ and N, respectively, can be built using Lagrange bases defined as

$$h_i(\xi) = \prod_{s=1, s\neq i}^{N} \left(\frac{\xi - \xi_s}{\xi_i - \xi_s} \right), \quad \text{and} \quad l_{i+1/2}(\xi) = \prod_{s=0, s\neq i}^{N} \left(\frac{\xi - \xi_{s+1/2}}{\xi_{i+1/2} - \xi_{s+1/2}} \right). \tag{2.5}$$

The reconstructed solution for the conserved variables in the standard element is then obtained as the tensor product of the three one-dimensional polynomials,

$$\overline{\boldsymbol{U}}(\boldsymbol{\xi}) = \sum_{k=1}^{N} \sum_{j=1}^{N} \sum_{i=1}^{N} \frac{\overline{\boldsymbol{U}}_{i,j,k}}{|J_{i,j,k}|} h_i(\xi_1) h_j(\xi_2) h_k(\xi_3), \tag{2.6}$$

where i, j and k are the indices of the solution points within each standard element. A similar reconstruction is adopted for the resolved fluxes $\overline{\boldsymbol{\mathcal{F}}}^k$.

The reconstructed fluxes are only element-wise continuous, but discontinuous across cell interfaces. For the inviscid flux, a Riemann solver is employed to compute a common flux at cell interfaces to ensure conservation and stability. In the current implementation, the Roe solver (Roe 1981) with entropy fix (Harten 1983) was used. The left and right states here represent the solution on both sides of the shared edge flux point. The viscous flux is a function of both the conserved variables and their gradients, and therefore the solution gradients have to be calculated at the flux points. The average approach described by Sun *et al.* (2007) is used to compute the viscous fluxes.

2.2. *LES modeling approach*

In order to close the SGS terms a structural model based on the scale similarity assumption (Bardina *et al.* 1980; Liu *et al.* 1994; Akhavan *et al.* 2000) is adopted. In the perspective of developing a similarity mixed formulation (Akhavan *et al.* 2000; Salvetti & Banerjee 1995; Anderson & Meneveau 1999; Zang *et al.* 1992, 1993; Erlebacher *et al.* 1992; Speziale 1985; Speziale *et al.* 1988) with correct near-wall scaling, a Wall-Adapting Local Eddy-viscosity (WALE) formulation (Nicoud & Ducros 1999) for the eddy-viscosity term was recently proposed by Lodato *et al.* (2009):

$$\tau_{ij}^{\mathrm{d}} = 2\overline{\rho}\nu_{\mathrm{sgs}}\widetilde{A}_{ij} - \overline{\rho}\big(\widehat{\widetilde{u}_i\widetilde{u}_j} - \widehat{\widetilde{u}}_i\widehat{\widetilde{u}}_j\big)^{\mathrm{d}}, \tag{2.7}$$

$$q_k = \gamma\overline{\rho}\kappa_{\mathrm{sgs}}\frac{\partial\widetilde{e_I}}{\partial x_k} - \gamma\overline{\rho}\big(\widehat{\widetilde{e_I}\widetilde{u}_k} - \widehat{\widetilde{e}}_I\widehat{\widetilde{u}}_k\big), \tag{2.8}$$

where $\widetilde{e_I}$ is the resolved internal energy and the *hat* operator represents filtering at cutoff length $\alpha\Delta$, with $\alpha \geq 1$ and sufficient localization in physical space (Liu *et al.* 1994). The SGS kinematic viscosity, ν_{sgs}, and thermal diffusivity, κ_{sgs}, are computed as (Nicoud &

Ducros 1999)

$$\nu_{\rm sgs} = C_{\rm w}^2 \Delta^2 \frac{(\widetilde{s}_{ij}^{\rm d} \widetilde{s}_{ij}^{\rm d})^{3/2}}{(\widetilde{S}_{ij}\widetilde{S}_{ij})^{5/2} + (\widetilde{s}_{ij}^{\rm d}\widetilde{s}_{ij}^{\rm d})^{5/4}}, \quad \text{and} \quad \kappa_{\rm sgs} = \frac{\nu_{\rm sgs}}{Pr_{\rm sgs}}, \tag{2.9}$$

where $C_{\rm w} = 0.5$, Δ is a measure of the grid cutoff length-scale, which is here evaluated following the same procedure as that suggested by Parsani *et al.* (2010), namely,

$$\Delta(\boldsymbol{\xi}) \sim \left[\frac{|\det(J(\boldsymbol{\xi}))|}{N^3}\right]^{1/3}, \tag{2.10}$$

$\widetilde{S}_{ij} = \frac{1}{2}(\partial\widetilde{u}_i/\partial x_j + \partial\widetilde{u}_j/\partial x_i)$ is the strain rate tensor of the resolved field and $\widetilde{s}_{ij}^{\rm d}$ is the traceless symmetric part of the square of the resolved velocity gradient tensor $\widetilde{g}_{ij} = \partial\widetilde{u}_i/\partial x_j$. The sub-grid scale Prandtl number, $Pr_{\rm sgs}$, is assumed constant and equal to 0.5 (Erlebacher *et al.* 1992; Speziale *et al.* 1988).

2.3. *Constrained discrete filters for the SD method*

Within the framework of similarity mixed SGS models, such as the WSM model used in this study, explicit filtering represents a key ingredient to approximate sub-grid scale interactions. This is done by assuming similarity within a narrow band of frequencies in the vicinity of the cutoff frequency k_c. As already mentioned in Section 2.2, similarity is assumed between the SGS scales and the smallest resolved scales, which are evaluated as the difference between the filtered and the twice-filtered field. Hence, the explicit filter should be designed (a) to have sufficient localization in physical space; (b) to ensure a certain selected cutoff length-scale. For instance, the box filter in physical space is generally used due to its locality and ease of implementation (Zang *et al.* 1993; Lodato *et al.* 2009). Lodato *et al.*, in particular, used a discrete approximation with cutoff length-scale $\widehat{\Delta} = 4/3\Delta$ according to what was proposed by Akhavan *et al.* (2000), as this filter width is an optimal size in order to sufficiently isolate the smallest resolved scales.

In order to develop a mixed similarity formulation to be applied with the SD method, the above ideas need to be generalized in a way which is numerically consistent with the use of SD elements. In particular, since the SGS model terms are evaluated at the flux points, the filtered quantities need to be evaluated at the same flux points starting from the discrete solution at the solution points. This can be achieved by filtering the solution at the solution points first, and then extrapolating the filtered quantities at the flux points using the same Lagrange polynomials used to reconstruct the fluxes [see Eq. (2.5)].

Considering for simplicity the one-dimensional SD element depicted schematically in Figure 1, a particularly desirable feature in building discrete filters is that the filter stencil does not lie across elements. Moreover, the non-uniform spacing of the solution points should be taken into account. The above considerations lead to the particularly challenging task of designing asymmetric non-uniform discrete filters with a fixed cutoff length-scale.

With regard to the SD element depicted in Figure 1, the discrete filtering operator for a generic quantity ϕ is defined as (Vasilyev *et al.* 1998)

$$\overline{\phi}_s = \sum_{i=1}^{N} w_i^s \phi_i, \quad (s = 1, \ldots, N), \tag{2.11}$$

where the s index refers to a quantity at the N solution points. For the case of hexa-

hedral elements as in the present study, the generalization to three dimensions follows immediately by the tensor product of 1D filtering operators.

The spectral signature of the above discrete filter is characterized by its associated transfer function in Fourier space (Berland *et al.* 2007), which is readily obtained as

$$\widehat{G}_s(k) = \sum_{i=1}^{N} w_i^s \exp(-\mathrm{j}\beta_i^s k\Delta), \quad \text{with} \quad \beta_i^s = \frac{\xi_i - \xi_s}{\Delta}, \tag{2.12}$$

where k is the wavenumber and $\mathrm{j} = \sqrt{-1}$; ξ_s represents the location of the solution points, whereas $\Delta = 1/N$ is assumed to be the actual resolution within the SD element [see Eq. (2.10)].

A possible strategy to build discrete filters can be devised by exploiting the resolution properties of polynomials of different order, thus performing the explicit filtering operation by applying the Restriction-Prolongation (RP) technique in each computational cell (Blackburn & Schmidt 2003; Premasuthan *et al.* 2009). Based on Eq. (2.12), for instance, the real part of the Fourier transform of the discrete filters constructed using the Restriction-Prolongation (RP) technique (Premasuthan *et al.* 2009) for $N = 3$ and 4 is plotted in Figure 2(a, b), where the box filter in physical space, with cutoff length equal to $4/3\Delta$, is also represented for reference. As is immediately evident, the cutoff frequency, namely, the frequency at which $\widehat{G}_s(k) \simeq 0.5$, for each solution point is different and thus the overall effective cutoff frequency is unpredictable. Furthermore, for $N = 4$, the most asymmetric filters, i.e., those represented with solid lines, have a relatively pronounced over-shoot in the low-frequency range, a feature which may lead to non-physical growth of energy (Vasilyev *et al.* 1998).

In order to overcome these problems, a Constrained Discrete (CD) filter satisfying a selected set of conditions, was developed for the SD method. The method used to derive these CD filters is based on the work of Vasilyev *et al.* (1998). In particular, starting from Eq. (2.12), the N filter weights w_i^s for the s-th solution point can be determined by providing N constraints. More precisely, a first obvious condition is related to the preservation of a constant variable, namely $\sum_{i=1}^{N} w_i^s = 1$. Then, starting from the idea of building filters whose kernels are as close as possible to that characterizing the box filter in physical space of width $\Delta_\mathrm{c} = \alpha\Delta$, the condition

$$\mathrm{Re}[\widehat{G}_s(k_\mathrm{c})] = \sum_{i=1}^{N} w_i^s \cos(\beta_i^s k_\mathrm{c}\Delta) = \left.\frac{\sin(k\Delta_\mathrm{c}/2)}{k\Delta_\mathrm{c}/2}\right|_{k=k_\mathrm{c}} = \frac{2}{\pi} \tag{2.13}$$

is enforced with $k_\mathrm{c} = \pi/\Delta_\mathrm{c}$, which therefore constrains the relevant cutoff length-scale. The remaining conditions are obtained by constraining the discrete filter to have $N - 2$ vanishing moments, thus achieving formal commutation with difference operators (Vasilyev *et al.* 1998).

The real part of the kernels of these CD filters for SD elements of order 3 and 4 are plotted in Figure 2(c, d).

As can be observed, these CD filters approximate the reference filter—the sharp cutoff in physical space—much more accurately than the RP filters in the low-frequency range, showing more pronounced deviations only at length-scales smaller than Δ (i.e. $k\Delta/\pi > 1$). However, recalling that $\Delta \sim O(1/N)$, these small scales are not expected to play a significant role as they are supposedly not supported by the actual resolution of the SD element. The actual cutoff frequency is also more predictable throughout the SD element. Moreover, the over-shoots observed in the asymmetric filters constructed by the

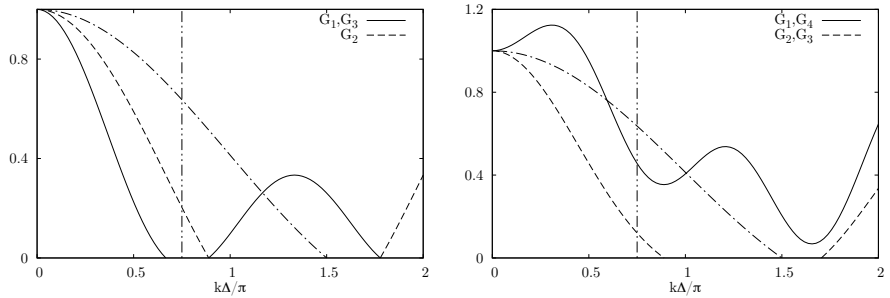

(a) RP filter, $N = 3$ (b) RP filter, $N = 4$

(c) CD filter, $N = 3$ (d) CD filter, $N = 4$

FIGURE 2. Real part of the transfer function $\widehat{G}(k\Delta/\pi)$ of RP (Premasuthan *et al.* 2009) and CD filters for different SD discretization orders N (—·— , analytical box filter in physical space). The vertical line indicates the cutoff length-scale at $4/3\Delta$.

RP method are now completely suppressed, hence a better numerical behavior in terms of stability is expected.

3. Results and discussion

In this section, the results obtained with the actual implementation WSM model are presented. Computations on two different geometries are reported: (a) channel flow at Reynolds numbers of 180 (based on the friction velocity and channel half-width); (b) flow past a confined circular cylinder at Reynolds number 2 580 (based on the upstream bulk velocity and cylinder diameter). For comparison, implicit LES computations without the SGS model were performed as well.

3.1. *Turbulent channel flow*

Two channel flow computations were performed at different orders ($N = 4$ and 5) at a Reynolds number $Re_\tau = 180$ (based on the friction velocity u_τ and channel half-width δ), and Mach number 0.3. The grid was $4\pi\delta$ long and $2\pi\delta$ wide and subdivided in 15^3 and 12^3 elements (uniformly spaced in the streamwise and spanwise directions and stretched with a hyperbolic tangent function in the vertical direction) for the computations with $N = 4$ and $N = 5$, respectively. The total number of Degrees of Freedom (DoF) was 216 000, and the grid resolution in wall units (namely, normalized by viscous length $\ell_\tau = \nu/u_\tau$) was $\Delta_x^+ \simeq 38$, $\Delta_y^+ \simeq 2.0$–10 (wall to centerline) and $\Delta_z^+ \simeq 19$ in the streamwise, vertical, and spanwise directions, respectively. Note that the resolution of the computation was

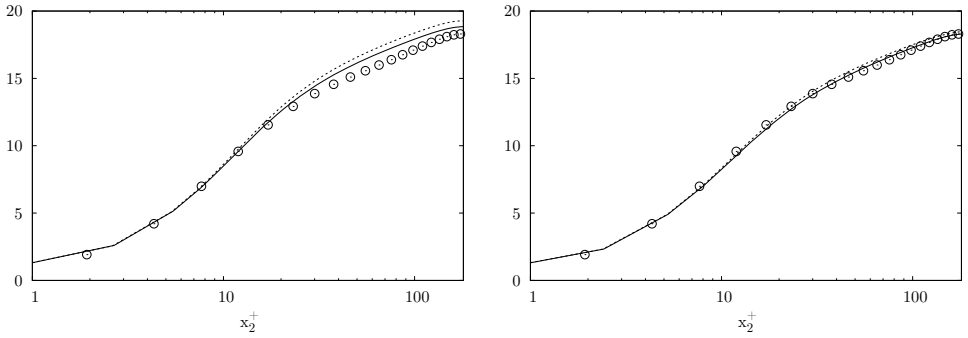

(CHN1) $Re_\tau = 180$, $N = 4$ (CHN2) $Re_\tau = 180$, $N = 5$

FIGURE 3. Mean streamwise velocity profile U^+: ——— , WSM model; ····· , no SGS model; ○ , DNS data (Moser *et al.* 1999).

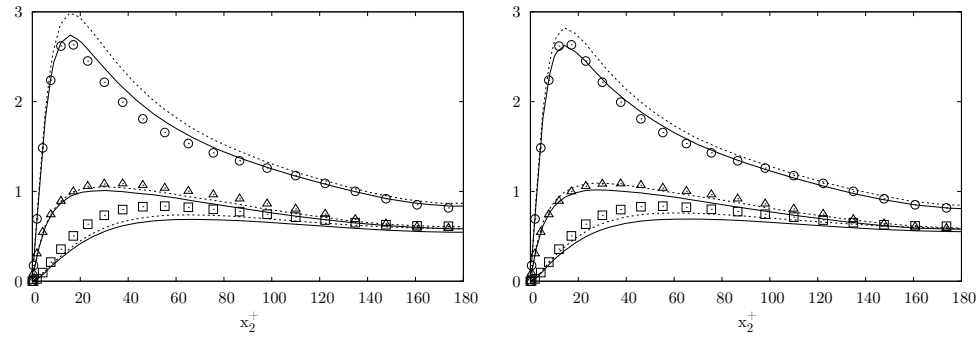

(CHN1) $Re_\tau = 180$, $N = 4$ (CHN2) $Re_\tau = 180$, $N = 5$

FIGURE 4. RMS of velocity fluctuations: ——— , WSM model; ····· , no SGS model; symbols, DNS data (Moser *et al.* 1999). ○ , $u^+_{\rm rms}$; □ , $v^+_{\rm rms}$; △ , $w^+_{\rm rms}$.

estimated as the actual element size divided by the number of solution points used within the element; in a Finite Volume (FV) context, this is equivalent to assuming that each element is filled with N^3 control volumes.

All the computations were performed with periodic boundary conditions in the streamwise and spanwise directions and no-slip isothermal walls were used on the top and bottom planes. In order to drive the flow, a source term $\mathcal{S}$ was added to the x_1 component of momentum. Given the compressible nature of the solver, in particular, $\mathcal{S}$ was determined at each time-step in order to equilibrate the instantaneous resultant shear at the wall, plus a relaxation term toward the expected mass flow rate to accelerate convergence. For consistency, another source term, computed using the bulk velocity as $u_{\rm b}\mathcal{S}$, was also added to the energy equation (isothermal walls were used to prevent the energy from increasing without bounds).

The computations were initialized with a uniform streamwise 4th-order velocity profile $u_1(\boldsymbol{x}) = \frac{15}{8}u_0\left[1-(x_2/\delta)^2\right]^2$ (u_0 is the reference velocity) and a perturbed vertical velocity component (Rossi 2009). After the flow field was fully developed and established, time averaging was performed for a period corresponding to about 18 flow-through times; further ensemble averaging in the streamwise and spanwise directions was also performed.

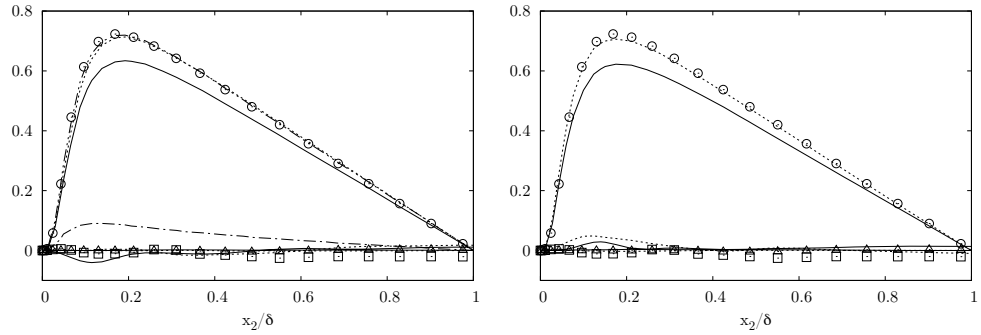

(CHN1) $Re_\tau = 180$, $N = 4$ (CHN2) $Re_\tau = 180$, $N = 5$

FIGURE 5. Reynolds shear stresses: ——— , WSM model; ····· , no SGS model; —·— , $\langle \tau_{12} \rangle$ from LES; —··— global shear stress from LES (resolved + SGS); symbols, DNS data (Moser *et al.* 1999). ○ , $-\langle u^+ v^+ \rangle$; □ , $-\langle u^+ w^+ \rangle$; △ , $-\langle v^+ w^+ \rangle$.

First- and second-order statistical moments are plotted in Figures 3–5, where the results from the explicit LES with the WSM model and the implicit LES are compared to the results from the Direct Numerical Simulations (DNS) performed by Moser *et al.* (1999). Note that the extremely small density variation ($\sim 1.4\%$ increase from centerline to the wall) did not make it necessary to use the Van Driest correction.

The behavior of the WSM model in reproducing the statistical features of the flow is quite satisfactory for each test case. With regards to the mean velocity profiles, the slope of the log law is correctly represented, whereas its intercept is slightly overestimated with respect to the DNS value. The higher order computation gives results in better agreement with the DNS data, even if the DoF and spatial resolution are the same. Overall, the use of the SGS model determines an improvement in the results obtained by implicit LES, which is more evident for the computations with four solution points per element. Reynolds stresses (see Figure 4) are more sensitive to the use of the SGS model, and implicit LES shows a marked tendency to overestimate velocity RMS fluctuations.

With regards to the root mean square (RMS) of the resolved velocity fluctuations, in particular, the profiles obtained with the use of the WSM model are in good agreement with the DNS data, regardless of the spatial discretization order. The location and intensity of the peak of streamwise velocity fluctuation is correctly captured. Spanwise and vertical fluctuations tend to be slightly underestimated.

The resolved turbulent shear stresses from the LES are always below the DNS curves, whereas the results from implicit LES are much closer (see Figure 5). Given the close connection between the mean streamwise velocity profile and the turbulent shear stress across the channel—the two quantities are strictly related through the steady Reynolds averaged x_1 momentum equation—and given the good agreement observed for the former quantity, it is here argued that the actual global turbulent shear from LES, namely, resolved + SGS modeled contribution, is in good agreement with its DNS counterpart. This is readily confirmed for test cases CHN1 by collecting the mean SGS shear stress $\langle \tau_{12} \rangle$ during the computation and by comparing the *exact* turbulent shear from DNS $\langle \overline{u}_1'^{\mathrm{e}} \overline{u}_2'^{\mathrm{e}} \rangle$ with the approximate global (resolved + SGS) turbulent shear from LES, i.e., $\langle \overline{u}_1' \overline{u}_2' \rangle + \langle \tau_{12} \rangle$ (Sagaut 2001). As can be observed in Figure 5 (CHN1), the approximate global turbulent shear matches the DNS data almost perfectly.

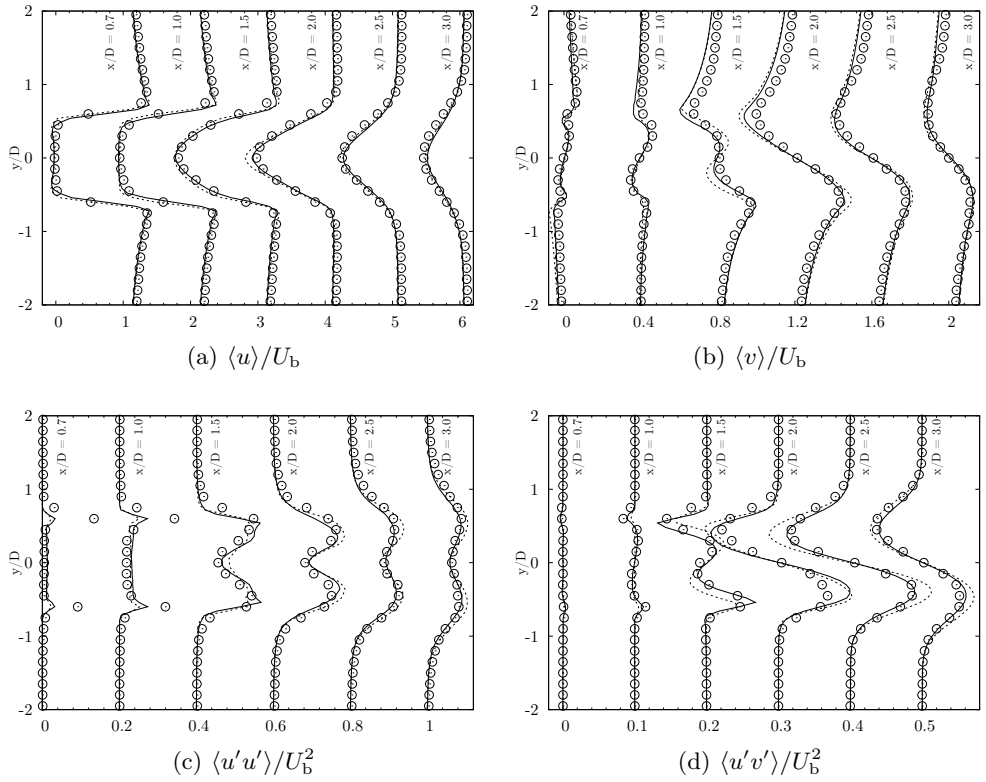

FIGURE 6. First- and second-order statistical moments of the resolved velocity field at different locations downstream of the cylinder: ——— , WSM model; ····· , no SGS model; ∘ , experimental PIV measurements by Konstantinidis *et al.* (2003, 2005) (every three points are represented).

3.2. *Flow past a circular cylinder*

The equations were integrated over an unstructured computational mesh of dimension $48D \times 10D \times 3.2D$ (L×H×W) with 47 976 hexahedral elements. Third-order (i.e., $N = 3$) accuracy was set. The simulations, an implicit LES and an explicit LES with the WSM model, were performed at Reynolds and Mach numbers of 2 580 and 0.25, respectively, based on the bulk velocity at the inlet U_b and the cylinder diameter D. The boundary conditions were periodic in the spanwise direction and no-slip adiabatic conditions were used on the top and bottom planes; the cylinder wall was set as no-slip adiabatic as well and the inflow/outflow conditions were imposed fixing the inlet density and velocity and the outlet pressure, respectively. The total number of DoF for each equation was about 1.3×10^6. Note that, compared to the resolution of the structured coarse mesh used by Mohammad *et al.* (2010) for a similar implicit LES computation, the resolution adopted here is about two times lower.

After the flow field was fully developed and established, statistics were performed averaging in time for 50–60 shedding periods; in view of the statistical two-dimensionality of the flow field, further ensemble averaging in the spanwise direction was also performed. Results were compared against Particle Image Velocimetry (PIV) experimental measurements (Konstantinidis *et al.* 2003, 2005).

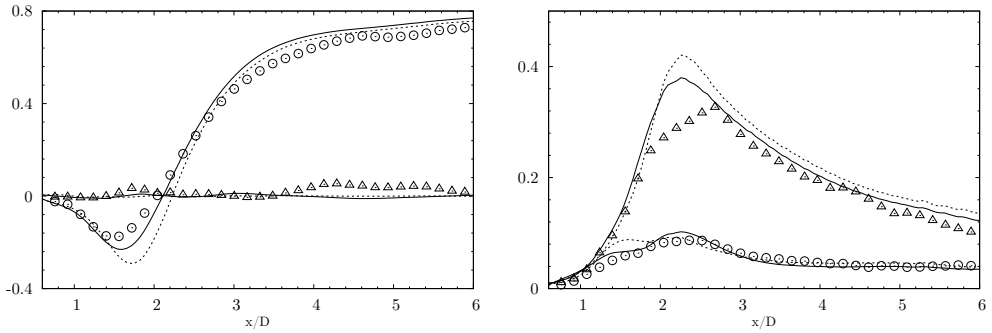

(a) $\langle u \rangle / U_\mathrm{b}$ and $\langle v \rangle / U_\mathrm{b}$ (b) $\langle u'u' \rangle / U_\mathrm{b}^2$ and $\langle v'v' \rangle / U_\mathrm{b}^2$

FIGURE 7. Streamwise and vertical mean (a) and fluctuations (b) of the resolved velocity measured along the wake of the cylinder at $y/D = 0$: ——— , WSM model; ····· , no SGS model; symbols (○ , streamwise; △ , vertical), experimental PIV measurements. (Konstantinidis *et al.* 2003, 2005)

First- and second-order statistical moments at different locations behind the cylinder and along the wake are plotted in Figures 6–7. The use of the SGS model produces, in general, better results mostly in terms of second-order statistical moments, as already observed for the channel flow computation.

4. Concluding remarks

Overall, the performances of the actual WSM model implementation in conjunction with the SD method are extremely satisfactory. Statistical moments are generally improved when the SGS model is used; the main benefit is a better representation of the Reynolds stresses. The proposed constrained discrete filter of arbitrary order proved to be numerically stable at any tested order (up to $N = 7$ in other tests not included here) and allows a relatively straightforward implementation into high-order SD schemes of any SGS model which relies upon the use of explicit filtering or dynamic procedures (Germano *et al.* 1991; Moin *et al.* 1991). Further development of wall modeling procedures and the unstructured nature of the high-order SD scheme will also allow relatively affordable high-fidelity LES computations in complex geometries.

Acknowledgments

The authors would like to thank Dr. J. Bodart, S.T. Bose, Prof. C. Liang and Dr. R. Rossi for stimulating and fruitful discussions.

REFERENCES

AKHAVAN, R., ANSARI, A., KANG, S. & MANGIAVACCHI, N. 2000 Subgrid-scale interactions in a numerically simulated planar turbulent jet and implications for modeling. *J. Fluid Mech.* **408**, 83–120.

ANDERSON, R. & MENEVEAU, C. 1999 Effects of the similarity model in finite-difference LES of isotropic turbulence using a Lagrangian dynamic mixed model. *Flow Turbul. Combust.* **62** (3), 201–225.

Bardina, J., Ferziger, J. & Reynolds, W. 1980 Improved subgrid-scale models for large-eddy simulation. *AIAA P. 1980-1357*.

Berland, J., Bogey, C., Marsden, O. & Bailly, C. 2007 High-order, low dispersive and low dissipative explicit schemes for multiple-scale and boundary problems. *J. Comput. Phys.* **224** (2), 637–662.

Blackburn, H. & Schmidt, S. 2003 Spectral element filtering techniques for large eddy simulation with dynamic estimation. *J. Comput. Phys.* **186** (2), 610–629.

Castonguay, P., Liang, C. & Jameson, A. 2010 Simulation of transitional flow over airfoils using the spectral difference method. *AIAA P. 2010-4626*.

Erlebacher, G., Hussaini, M., Speziale, C. & Zang, T. 1992 Toward the large-eddy simulation of compressible turbulent flows. *J. Fluid Mech.* **238**, 155–185.

Germano, M., Piomelli, U., Moin, P. & Cabot, W. 1991 A dynamic subgrid-scale eddy viscosity model. *Phys. Fluids A-Fluid* **3** (7), 1760–1765.

Harten, A. 1983 High resolution schemes for hyperbolic conservation laws. *J. Comput. Phys.* **49** (3), 357–393.

Hesthaven, J. & Warburton, T. 2007 *Nodal Discontinuous Galerkin Methods: Algorithms, Analysis, and Applications*. Springer Verlag.

Huynh, H. 2007 A flux reconstruction approach to high-order schemes including discontinuous Galerkin methods. *AIAA P. 2007-4079*.

Karniadakis, G. & Sherwin, S. 1999 *Spectral/hp Element Methods for CFD*. Oxford University Press, USA.

Konstantinidis, E., Balabani, S. & Yianneskis, M. 2003 The effect of flow perturbations on the near wake characteristics of a circular cylinder. *J. Fluid. Struct.* **18** (3-4), 367–386.

Konstantinidis, E., Balabani, S. & Yianneskis, M. 2005 Conditional averaging of PIV plane wake data using a cross-correlation approach. *Exp. Fluids* **39** (1), 38–47.

Kopriva, D. & Kolias, J. 1996 A conservative staggered-grid Chebyshev multidomain method for compressible flows. *J. Comput. Phys.* **125** (1), 244–261.

Lesieur, M., Métais, O. & Comte, P. 2005 *Large-Eddy Simulations of Turbulence*. Cambridge University Press.

Liang, C., Jameson, A. & Wang, Z. 2009*a* Spectral difference method for compressible flow on unstructured grids with mixed elements. *J. Comput. Phys.* **228** (8), 2847–2858.

Liang, C., Premasuthan, S. & Jameson, A. 2009*b* High-order accurate simulation of low-Mach laminar flow past two side-by-side cylinders using spectral difference method. *Comput. Struct.* **87** (11-12), 812–827.

Liang, C., Premasuthan, S., Jameson, A. & Wang, Z. 2009*c* Large eddy simulation of compressible turbulent channel flow with spectral difference method. *AIAA P. 2009-402*.

Liu, S., Meneveau, C. & Katz, J. 1994 On the properties of similarity subgrid-scale models as deduced from measurements in a turbulent jet. *J. Fluid Mech.* **275**, 83–119.

Liu, Y., Vinokur, M. & Wang, Z. 2006 Spectral difference method for unstructured grids I: basic formulation. *J. Comput. Phys.* **216** (2), 780–801.

Lodato, G., Vervisch, L. & Domingo, P. 2009 A compressible wall-adapting similarity mixed model for large-eddy simulation of the impinging round jet. *Phys. Fluids* **21** (3), 035102.

May, G. & Jameson, A. 2006 A spectral difference method for the Euler and Navier-Stokes equations on unstructured meshes. *AIAA P. 2006-304*.

Mohammad, A., Wang, Z. & Liang, C. 2010 Large eddy simulation of flow over a cylinder using high-order spectral difference method. *Adv. Appl. Math. Mech.* **2** (4), 451–466.

Moin, P., Squires, K., Cabot, W. & Lee, S. 1991 A dynamic subgrid-scale model for compressible turbulence and scalar transport. *Phys. Fluids A-Fluid* **3** (11), 2746–2757.

Moser, R., Kim, J. & Mansour, N. 1999 Direct numerical simulation of turbulent channel flow up to $\mathrm{Re}_\tau = 590$. *Phys. Fluids* **11** (4), 943–945.

Nicoud, F. & Ducros, F. 1999 Subgrid-scale stress modelling based on the square of the velocity gradient tensor. *Flow Turbul. Combust.* **62** (3), 183–200.

Ou, K., Liang, C., Premasuthan, S. & Jameson, A. 2009 High-order spectral difference simulation of laminar compressible flow over two counter-rotating cylinders. *AIAA P. 2009-3956*.

Parsani, M., Ghorbaniasl, G., Lacor, C. & Turkel, E. 2010 An implicit high-order spectral difference approach for large eddy simulation. *J. Comput. Phys.* **229** (14), 5373–5393.

Premasuthan, S., Liang, C. & Jameson, A. 2009 A spectral difference method for viscous compressible flows with shocks. *AIAA P. 2009-3785*.

Roe, P. 1981 Approximate Riemann solvers, parameter vectors, and difference schemes. *J. Comput. Phys.* **43**, 357–372.

Rossi, R. 2009 Direct numerical simulation of scalar transport using unstructured finite-volume schemes. *J. Comput. Phys.* **228** (5), 1639–1657.

Sagaut, P. 2001 *Large Eddy Simulation for Incompressible Flows: An Introduction*, 2nd edn. Springer-Verlag Berlin Heidelberg.

Salvetti, M. & Banerjee, S. 1995 *A priori* tests of a new dynamic subgrid-scale model for finite-difference large-eddy simulations. *Phys. Fluids* **7** (11), 2831–2847.

Speziale, C. 1985 Galilean invariance of subgrid-scale stress models in the large-eddy simulation of turbulence. *J. Fluid Mech.* **156**, 55–62.

Speziale, C., Erlebacher, G., Zang, T. & Hussaini, M. 1988 The subgrid-scale modeling of compressible turbulence. *Phys. Fluids* **31** (4), 940–942.

Sun, Y., Wang, Z. & Liu, Y. 2007 High-order multidomain spectral difference method for the Navier-Stokes equations on unstructured hexahedral grids. *Commun. Comput. Phys.* **2** (2), 310–333.

Vasilyev, O., Lund, T. & Moin, P. 1998 A general class of commutative filters for LES in complex geometries. *J. Comput. Phys.* **146** (1), 82–104.

Wang, Z., Liu, Y., May, G. & Jameson, A. 2007 Spectral difference method for unstructured grids II: Extension to the Euler equations. *J. Sci. Comput.* **32** (1), 45–71.

Zang, T., Dahlburg, R. & Dahlburg, J. 1992 Direct and large-eddy simulations of three-dimensional compressible Navier-Stokes turbulence. *Phys. Fluids A-Fluid* **4** (1), 127–140.

Zang, Y., Street, R. L. & Koseff, J. R. 1993 A dynamic mixed subgrid-scale model and its application to turbulent recirculating flows. *Phys. Fluids A-Fluid* **5** (12), 3186–3196.